Crystal-chemistry and temperature behavior of the natural hydrous borate colemanite, a mineral commodity of boron

Paolo Lotti[1,2,*], G. Diego Gatta[1,3], Nicola Demitri[2], Giorgio Guastella[4], Silvia Rizzato[5], Marco Aldo Ortenzi[5,6], Fabrizio Magrini[1], Davide Comboni[1], Alessandro Guastoni[7], Maria Teresa Fernandez-Diaz[8]

[1] Dipartimento di Scienze della Terra, Università degli Studi di Milano, Via Botticelli 23, 20133 Milano, Italy

[2] Elettra Sincrotrone Trieste S.c.P.A., Strada Statale 14 km 163.5, 34149 Basovizza, Trieste, Italy

[3] CNR-Istituto di Cristallografia, Sede di Bari, Via Amendola 122/O, 70126 Bari, Italy

[4] Agenzia delle Dogane e dei Monopoli, Direzione Regionale per la Lombardia, Laboratorio e Servizi Chimici, Via Marco Bruto 14, 20138 Milano, Italy

[5] Dipartimento di Chimica, Università degli Studi di Milano, Via Golgi 19, 20122 Milano, Italy

[6] CRC Materiali Polimerici "LaMPo", Dipartimento di Chimica, Università degli Studi di Milano, Via Golgi 19, 20122 Milano, Italy

[7] Dipartimento di Geoscienze, Università degli Studi di Padova, Via Gradenigo 6, 35131 Padova, Italy

[8] Institut Laue-Langevin, 71 Avenue des Martyrs, 38042 Grenoble-Cedex 9, France

* Corresponding Author: paolo.lotti@unimi.it; +390250315598 (Tel); +390250315597 (fax)

Abstract

Colemanite, $CaB_3O_4(OH)_3 \cdot H_2O$, is the most common hydrous Ca-borate, as well as a major mineral commodity of boron. In this study, we report a thorough chemical analysis and the low-temperature behavior of a natural sample of colemanite, by means of a multi-methodological approach. From the chemical point of view, the investigated sample resulted to be relatively pure, its composition being very close to the ideal one, with only a minor substitution of Sr^{2+} for Ca^{2+}. At about 270.5 K a displacive phase transition from the centrosymmetric $P2_1/a$ to the acentric $P2_1$ space group occurs. On the basis of in situ single-crystal synchrotron X-ray (down to 104 K) and neutron diffraction (at 20 K) data, the hydrogen-bonding configuration of both the polymorphs and the structural modifications at the atomic scale at varying temperatures are described. The asymmetric distribution of ionic charges along the [010] axis, allowed by the loss of the inversion center, is likely responsible for the reported ferroelectric behavior of colemanite below the phase transition temperature.

Keywords

Colemanite, borates, low-temperature, phase transition, neutron diffraction, synchrotron, ferroelectric behavior.

1. Introduction

Borates are nowadays important industrial minerals with main applications in the fields of glass and ceramic industries (for improving chemical and thermal properties or as fluxing agents), fertilizers and detergents production (Crangle 2015). During the last decade, the world borates production substantially doubled from 4750 thousand metric tons in 2006 (U.S. Geological Survey 2007) to 9400 thousand metric tons in 2016 (excluding US production, U.S. Geological Survey 2017), with Turkey being the leading producer sharing more than 50% of the world production. Despite more than 250 boron-containing mineralogical species exist, only four of them are presently of major economic importance as mineral commodities: borax, colemanite, ulexite and kernite (Crangle 2015).

Colemanite, $CaB_3O_4(OH)_3 \cdot H_2O$, is the most important Ca-borate and is currently extracted mainly from the Emet and Bigadiç deposits (Turkey), as a commodity for B_2O_3 and for the production of Na-free fiberglass (Helvaci 2015). Economically exploitable colemanite deposits usually occur for chemical precipitation of this mineral from relatively diluted waters of lacustrine basins, hosted in continental semi-arid to arid environments and fed by B-rich hydrothermal springs related to a local volcanic activity (Helvaci 1995, 2015; Garret 1998; Helvaci and Alonso 2000). In the last years, the large availability of colemanite as an economic raw material triggered several researches aimed to explore the potential applications of this mineral in different technological processes, a short list of which can be found, e.g., in Lotti et al. (2017).

The crystal structure of colemanite was first solved by Christ et al. (1954) and later refined by Christ et al. (1958) and Clark et al. (1964) by means of single-crystal X-ray diffraction data. It is characterized by infinite chains of B-coordination polyhedra running along the [100] direction. These chains are built by the repetition of corner-sharing rings, each made by three polyhedra: one BO_3 triangle and two $B\phi_4$ (ϕ = O, OH) tetrahedra (Figure 1). Along the [001] axis, the chains of B-

3

62 polyhedra are connected through chains of corner-sharing Ca-coordination polyhedra (Figure 1),

63 giving rise to hetero-polyhedral sheets perpendicular to [010]. The connection among adjacent

64 sheets along [010] is granted by two Ca-O(H)-B bonds per unit cell and by an extensive network of

65 H-bonds (Figure 1), which is responsible for the perfect (010) cleavage observed in colemanite

66 crystals. A model for the hydrogen positions was first proposed by Christ et al. (1954) and Clark et

67 al. (1964), based on interatomic oxygen-oxygen distances, and was later refined by Hainsworth and

68 Petch (1966) and Burns and Hawthorne (1993), on the basis of single-crystal neutron and X-ray

69 diffraction data, respectively. A discussion on the structure model of colemanite including the

70 hydrogen atoms is given in section 1.2.

71 A second-order phase transition from the paraelectric colemanite, stable at ambient conditions, to a

72 ferroelectric, pyroelectric and piezoelectric polymorph is long-time known to occur in the T-range

73 between 273 and 261 K (Chynoweth 1957; Wieder 1959: Wieder et al. 1962; Fenzl and Shuppler

74 1994; Slabkaya et al. 2004; Gavrilova et al. 2006). The displacive phase transition from the

75 centrosymmetric $P2_1/a$ space group to the acentric $P2_1$ was suggested by Perloff and Block (1960),

76 based on the analysis of systematic extinctions in single-crystal X-ray diffraction patterns collected

77 before and after the transition, and later confirmed by Hainsworth and Petch (1966), by means of

78 neutron diffraction data collected at ambient T and 253 K, respectively. Wieder et al. (1962) found

79 that for a pure synthetic colemanite the phase transition occurred at 233 K (vs. 261 K for a natural

80 sample investigated by the same authors) and suggested that small chemical impurities (namely, the

81 substitution of Sr^{2+} for Ca^{2+}) are responsible for the different experimentally determined phase-

82 transition temperatures. In particular, the higher the deviation from the ideal $CaB_3O_4(OH)_3 \cdot H_2O$

83 composition, the higher the temperature of the phase transition (and the larger the stability field of

84 the ferroelectric $P2_1$-colemanite).

85 Despite the early structural studies on colemanite date back to half a century ago and the recent

86 technological interest triggered by the economic importance as a bulk commodity, several open

4

87   questions persist about the crystal structure of this mineral and its behavior at non-ambient

88   conditions. In this light, our group has recently published a study on the high-pressure behavior of

89   colemanite, by means of in situ single-crystal synchrotron X-ray diffraction experiments using a

90   diamond anvil cell (Lotti et al. 2017), showing that this natural hydrous borate undergoes a

91   reconstructive phase transition at ca. 14.5 GPa, with an increase of the average coordination number

92   of both the B and Ca sites. In particular, a fraction of the boron cations increases its coordination

93   from triangular to tetrahedral, by making new bonds with H_2O-oxygen atoms (Lotti et al. 2017). In

94   this study, using in situ single-crystal synchrotron X-ray diffraction and differential scanning

95   calorimetry techniques, we inspect the low-temperature behavior of colemanite and the paraelectric-

96   to-ferroelectric phase transition, reporting, to the best of our knowledge for the first time, the *T*-

97   induced structural evolution down to 104 K. In addition, a single-crystal neutron diffraction

98   experiment at 20 K was performed to resolve the uncertainties concerning the hydrogen positions

99   below the transition temperature (see section 1.2). Recently, the potential role of colemanite as a

100 host for pollutants (e.g., arsenic, Lin et al. 2011) or metals of economic relevance (e.g., REE,

101 Helvaci et al. 2017) has been studied. In this light, and taking into account the potential influence of

102 chemical impurities on the phase stability field of the ferroelectric polymorph (Wieder et al. 1962),

103 we have conducted a thorough chemical characterization of the studied natural sample of

104 colemanite. In particular, adopting a multi-methodological approach, the presence and abundance of

105 more than 50 chemical species have been investigated, to carefully determine the chemical

106 composition of our sample.

107 This work belongs to a larger study of the phase stability and of the elastic and structural behavior

108 of borate compounds, both natural and synthetic, at non-ambient conditions (e.g., Gatta et al. 2010a,

109 2010b, 2011, 2013, 2017).

110

111 **1.1. The crystal structure of colemanite: the hydrogen positions**

112 The crystal-structure models of the paraelectric (space group $P2_1/a$) and ferroelectric (space group

113 $P2_1$) polymorphs of colemanite have been reported and discussed by Hainsworth and Petch (1966),

114 based on structure refinements from neutron diffraction data collected at ambient temperature and

115 253 K, respectively. From the ambient data of the $P2_1/a$ colemanite, the authors report the presence

116 of diffuse residues in the difference-Fourier syntheses of nuclear densities close to the position of

117 the H99 (H5 in this work) and H54 (H2 in this work) atoms, which are interpreted as due to the split

118 of these two hydrogens in two different positions [from this point, we will make use only of the

119 notation of Burns and Hawthorne (1993) to refer to atomic positions: O9, H96, H99, O5, H54 in

120 Hainsworth and Petch (1966) are, respectively, Ow8, H4, H5(A,B), O2 and H2 in this work]. In

121 fact, in the colemanite structure two H_2O molecules are symmetry-related through the inversion

122 center (Figure 2). However, due to steric hindrance, only the hydrogen (in position "A", H5A) of

123 one molecule may act as a bridge between the two oxygen atoms, the hydrogen of the second

124 molecule being forced to occupy a position "B", where it can form H-bonds to different framework

125 oxygens. According to Hainsworth and Petch (1966), the position of the hydrogen in A or B slightly

126 affects also the position of the closer Ca cation, which is attracted to or rejected from the Ow8 site

127 depending on whether it is shielded or not by the positive charge of H5B. In turn, according to the

128 authors, the position adopted by Ca induces the H2 atom in one of two mutually exclusive

129 configurations (labelled "C" and "D"). In the $P2_1/a$ structure, the presence of the inversion center

130 implies that both the adjacent water molecules statistically donate the H5 atom in bridging position

131 A. This condition can be accomplished by a dynamical disorder of the H5 and H2 atoms, which

132 continuously flip among the two alternative and mutually exclusive configurations. The $P2_1/a$-to-

133 $P2_1$ phase transition, with the loss of the inversion center, changes such a condition. As a

134 consequence, based on neutron diffraction data collected at 253 K, Hainsworth and Petch (1966)

135 reported the ordering of the hydrogens in one of the two possible configurations, so that, e.g., if an

136 H5 atom freezes in the A position, the adjacent H_2O molecule will display H5 in B configuration.

137 Through the influence on the Ca positions, the ordering of H5 will also imply the ordering of the H2

138 atoms all over the crystal. The shift from a dynamical disorder to a static ordering of the hydrogen

139 atoms at the phase transition was also suggested by Holuj and Petch (1960), based on proton

140 resonance analysis, from which the freezing of some proton motions was inferred.

141 It is worth to report that a different model was proposed by Burns and Hawthorne (1993) for the

142 hydrogen positions of colemanite at ambient conditions, by means of single-crystal X-ray

143 diffraction data. According to these authors, both the H_2O molecules contribute to the H-bonding in

144 a four-bond "donor-acceptor-donor-acceptor ($\cdots$O-H$\cdots$O-H$\cdots$)" ring configuration.

145

2. Materials and experimental methods

2.1 Colemanite sample and mineralogy

148 This study was performed on a gem-quality sample of natural colemanite from the borate deposits

149 of the Bigadiç Mine (Balikesir Province, Marmara Region, Turkey), provided by the Museum of

150 Mineralogy of the University of Padua (catalogue number MMP M14738). The colemanite and

151 ulexite deposits of the Bigadiç area were formed under evaporitic conditions in arid climate for the

152 precipitation of the borates in Neogene saline lakes, fed by both hydrothermal fluids related to an

153 underlying volcanism and streams weathering the neighboring volcanic rocks (Helvaci 1995).

154 Colemanite is reported by Helvaci (1995) to be of primary genesis, precipitating from the brine both

155 within unconsolidated sediments and, later, in veins and vugs.

156

2.2 Chemical analysis

158 The pure monomineralic nature and the relative abundance of the colemanite samples used for this

159 study, validated by optical analysis, allowed a thorough chemical investigation using a multi-

160 methodological approach, with a comprehensive survey of more than 50 chemical species. Boron

and calcium contents have been determined by adopting titrimetric methods. Thermal

decomposition and infrared absorption have been adopted to determine the amount of carbon and

hydrogen. Fluorine has been measured by ion selective electrode technique, whereas chloride,

bromide and iodide by ion chromatography. Inductive coupled plasma atomic emission

spectroscopy (ICP-AES) has been used to determine the weight fractions of minor elements. The

H_2O content has been determined by weight loss upon heating. A detailed description of the

combined experimental techniques adopted for the chemical analysis is given in Appendix I. The

full results are reported in Tables S1-S7 (supplementary materials). The chemical composition of

the studied colemanite, referred to the major elements, is reported in Table 1.

2.3 Differential scanning calorimetry

DSC analyses were conducted using a Mettler Toledo DSC1 apparatus with the samples sealed in

aluminum crucibles (6.31 mg mass). The thermal transition was studied in detail by performing the

following temperature cycles:

1. Heating from 233 to 423 K at 10 K/min;

2. 5 minutes isotherm at 423 K;

3. Cooling from 423 to 233 K at 10 K/min;

4. 5 minutes isotherm at 233 K;

5. Heating from 233 to 423 K at 10 K/min;

The initial heating to 423 K and the subsequent isothermal stage, i.e. cycles 1 and 2, were carried

out to *remove* adsorbed surface water or moisture that could give a small endothermic peak in the

temperature range of interest.

183 Since irreversible phase changes and/or transitions do not occur in both heating and cooling cycles,

184 a subsequent heating cycle, i.e. cycle 5, was performed to assess the reversible nature of the thermal

185 phenomena observed during the first heating.

186

2.4 Low-temperature X-ray diffraction

188 The low-temperature X-ray diffraction experiments were performed at the X-ray Diffraction

189 beamline (XRD1, Lausi et al. 2015) of the Elettra synchrotron source at Trieste, Italy. A colorless

190 platy crystal was dipped in NHV oil (Jena Bioscience GmbH) and mounted on the goniometer head

191 with a nylon loop. Complete datasets were collected at different temperatures (Table 2), through the

192 rotating crystal method, using a nitrogen stream from an Oxford Cryostream 700 series cryostat.

193 Data were acquired using a monochromatic wavelength of 0.700 Å on a Pilatus 2M hybrid-pixel

194 area detector. The diffraction data were indexed and integrated using the XDS software (Kabsch

195 2010). The structure refinements were performed using the JANA2006 software (Petriček et al.

196 2014) starting from the model of Burns and Hawthorne (1993), excluding the hydrogen atoms,

197 which were located by difference-Fourier syntheses. All the refinements were performed using

198 anisotropic displacements parameters (dp's), except for the H atoms, which were restrained to share

199 the same isotropic dp. A soft restriction on the O-H distances (0.85 ±0.02 Å) was applied. The

200 structure of the low-T polymorph of colemanite in the $P2_1$ space group has been derived according

201 to the group-subgroup relationship. The same restrictions reported for the $P2_1/a$ polymorph were

202 applied to the least-squares refinement of $P2_1$-colemanite, except for the following: due to unstable

203 refinements, the displacement parameters of all the boron and of the O51 and O52 sites (also O11

204 and O12 for the refinement based on the data collected at 260 K) were restrained to be isotropic.

205 Statistical data of the structure refinements and selected structural parameters are reported in Tables

206 2 and 3, respectively. The refined structure models at 300 and 104 K are reported in Table 4. The

207 fully refined structure models are deposited as supplementary materials.

2.5 Neutron diffraction experiment at 20 K

A prismatic crystal of colemanite (1.8 x 3.8 x 5.4 mm^3), free of defects under the polarised optical microscope, was selected for the neutron diffraction experiment. Neutron-diffraction data were measured at 20 K on the four-circle diffractometer D9, at the high-flux research reactor of the Institut Laue-Langevin (ILL) in Grenoble, France, with a neutron beam of wavelength 0.8390(2) Å, obtained by reflection from a Cu(220) monochromator. The D9 diffractometer is equipped with a small two-dimensional area detector (Lehmann et al. 1989), which allowed optimum resolution of the peaks from the background. Diffraction data were collected up θ_{max} of 31° (h, k, l ranges are listed in Table 2). For all data, background corrections following Wilkinson et al. (1988) and Lorentz corrections were applied. Absorption corrections were made by Gaussian integration (Coppens et al. 1965), using the calculated attenuation coefficient with account taken for the wavelength dependence of the absorption for the hydrogen content (Howard et al. 1987). Initial structure refinements showed that extinction affected only a few reflections, and could be well accounted for by the simple isotropic extinction model in JANA2006 (Petriček et al. 2014). The low degree of extinction meant that the data could be averaged over symmetry-equivalent reflections. The 2724 reflections scanned gave 1923 unique reflections with an internal discrepancy index of 0.0507 (averaging in the 2/m Laue class). Since the three-dimensional count distribution around each reflection was observed, the centroids of all scanned reflections could be found. Least-squares matching of the observed and calculated centroids of a few hundreds of the strongest reflections gave the lattice constants listed in Table 2. The reflection conditions suggested the space group $P2_1$. Other details pertaining to the neutron data collections are listed in Table 2.

The structure refinement was performed based on the model of $P2_1$-colemanite refined at 104 K from X-ray diffraction data, except for the hydrogen positions, which were independently located by difference-Fourier syntheses. The Ca, O (except Ow), H_2O-oxygens and H atoms were constrained to share the same isotropic displacement parameter, respectively. Statistical data on the

10

233 structure refinement and selected structural parameters are reported in Tables 2, 4 and 5,

234 respectively.

235

236 **3. Results and discussion**

237 **3.1 Chemical composition**

238 The chemical composition of the sample of colemanite of this study has been thoroughly

239 investigated: the presence and relative abundance of 57 chemical species, including major and trace

240 elements, have been described by means of a multi-methodological approach (see section 2.2 and

241 Appendix I). The full results of the chemical analyses are reported in Tables S1-S7 (supplementary

242 material), whereas the composition of the most relevant chemical constituents is reported in Table

243 1. The relative purity of the colemanite sample, confirmed by the results of the ICP-AES analysis,

244 allowed the use of simple titrimetric methods for the determination of the B_2O_3 and CaO contents.

245 In particular, in the absence of cations such as Fe and Al, the acid-base titration with mannitol

246 provides the exact amount of boron entirely present as H_3BO_3 in acid environment. For the

247 determination of calcium it was not necessary to add any masking agent or precipitant before the

248 titration. The results show that, except for a minor substitution of Ca^{2+} by Sr^{2+} (Table 1), any other

249 trace element is below the detection limit ranging between 100 and 500 ppm. Within the scope of

250 this study, i.e. the characterization of the crystal chemistry of colemanite at ambient and non-

251 ambient conditions, we can conclude that the selected natural sample is virtually ideal, being the

252 composition very close to the nominal one: $Ca_{0.99}Sr_{0.01}B_{3.00}O_4(OH)_{3.00} \cdot 0.99H_2O$. The minimum

253 content of SiO_2, measured from ICP-AES analysis (Tables 1 and S5), may be attributed either to a

254 substitution of tetrahedral B by Si, or to a minor amount of silicate-mineral impurities within the

255 massive sample.

256

3.2 Crystal structure of the $P2_1/a$-colemanite at ambient conditions

The structure refinement performed on the basis of the X-ray diffraction data collected at 300 K substantially confirms the model proposed by Hainsworth and Petch (1966). Despite the intrinsically weak X-ray scattering factor of hydrogen (Wilson and Prince 1999), the difference-Fourier syntheses of electron density, based on H-free structure refinements, allowed the location of the hydrogen positions. As expected, three peaks were found close to the H_2O oxygen atom: the most intense corresponding to the H4 site and the remaining to two mutually exclusive configurations of H5 (see section 1.2) (Figure 2; Table 4). A diffuse residue was found at the expected position for the H2 atom. Any attempt to refine two split and mutually exclusive sites, according to the model of Hainsworth and Petch (1966), failed. Therefore, the refined H2 coordinates (Table 4) must be interpreted as the barycentric position of a dynamically disordered atom. The hydrogen bonding network of colemanite is reported in Table 5. As previously mentioned by Hainsworth and Petch (1966), the hydrogen atoms in position H2 and H5B are generically oriented towards a region where they can make alternative bonds with the framework oxygens (Figure 2; Table 5).

3.3 The paraelectric to ferroelectric phase transition.

The phase transition from the (high-temperature) paraelectric $P2_1/a$-colemanite to the (low-temperature) ferroelectric $P2_1$-polymorph has been investigated by means of differential-scanning calorimetry and in situ low-temperature single-crystal X-ray diffraction.

The differential scanning calorimetry analysis (Figures 3 and 1S, supplementary material) confirms that a reversible transition takes place and this is consistent with the structural modifications, corresponding to an enantiotropic phase transition, observed by X-ray diffraction (Giron 1995; Kawakami 2007). In the first heating cycle the thermogram exhibits a weak endothermic peak

12

281 centered at about 270.5 K (-2.5 °C) with an onset temperature of about 263 K (-10°C) and an endset

282 temperature around 275 K (2°C) (Figure 3). In the successive cooling step, an exothermal transition

283 is observed over the same temperature range while in the final heating cycle an endothermic event

284 analogous to that observed in the first cycle is reproduced (Figure 3). No hysteresis phenomena are

285 detected as clearly shown in Figure 3.The heat involved in the transition is clearly very low (less

286 than 0.4 J/g) but it cannot be determined with high accuracy given the relatively unstable baseline in

287 proximity of the transition itself. An estimation is provided in Figure 3.

288 The single-crystal X-ray diffraction datasets, collected at low temperature, have been investigated

289 following the intensities of the classes of reflections systematically absent in the $P2_1/a$ space group,

290 i.e.:

291   • $h00$, for $h = 2n +1$

292   • $0k0$, for $k = 2n +1$

293   • $h0l$, for $h = 2n +1$.

294 The $P2_1/a$-to-$P2_1$ phase transition can be identified since in the latter space group no reflection

295 conditions apply to $h00$ and $h0l$, in contrast to the $0k0$ peaks, which keep the extinction conditions

296 for $k = 2n +1$. Table 6 shows the average intensities of these classes of reflections at varying

297 temperatures, as well as the number of peaks violating the extinction conditions according to three

298 different cut-off criteria: $I_{hkl}/\sigma(I_{hkl}) \geq 1$, ≥ 3 and ≥ 6, respectively. A reconstruction of the $h0l$*

299 reciprocal lattice planes, based on the data collected at 300 and 104 K, respectively, is reported in

300 Figure 4. The results reported in Table 6 show a discontinuity between 265 and 260 K, which is

301 followed by an increasing number of violating reflections with decreasing temperature, as can be

302 detected in Figure 4.

303 These results confirm that the phase transition is displacive in character, from the centrosymmetric

304 $P2_1/a$ space group to the acentric $P2_1$ subgroup, and does not induce the occurrence of any

13

spontaneous strain (Figure 5). The differential scanning calorimetry results show that this phase transition occurs in the range between 263 and 275 K. The slightly lower temperature range derived from the X-ray diffraction data can be attributed to the difficulties in recognizing the phase transition temperature relying only on the systematic extinctions.

The loss of the glide plane and of the related inversion center provides the structural basis for the ferro-, pyro- and piezo-electric behavior of colemanite at low temperatures, as already reported by Perloff and Block (1960) and Hainsworth and Petch (1966). In the following sections, we report, to the best of our knowledge for the first time, the elastic and structural evolution of the ferroelectric polymorph of colemanite at varying temperatures down to 104 K.

3.4 Low-temperature elastic behavior

The evolution of the unit-cell volume and linear parameters of colemanite as a function of temperature, based on X-ray diffraction data, are reported in Figure 5 and Table 2. Apparently, the elastic behavior of colemanite is unaffected by the occurrence of the phase transition. In this light, the experimental volume data were fitted with a Berman T-V equation of state within the entire T-range investigated using the *EoSFit7-GUI* software (Gonzalez-Platas et al. 2016). The following parameters were refined adopting a reference temperature of 298 K: $V_0 = 560.3(1)$ Å^3, $\alpha_0 = 4.4(6) \cdot 10^{-5}$ K^{-1} and $\alpha_1 = 8(7) \cdot 10^{-8}$ K^{-2}, for which the thermal expansion coefficients predicted at 298 and 104 K, respectively, are: $\alpha_{V298K} = \alpha_0$ and $\alpha_{V104K} = 2.8(7) \cdot 10^{-5}$ K^{-1}.

The unit-cell linear parameters, reported in Table 2 and Figure 5, show that the volume reduction with decreasing temperature is accommodated along the b and c axes, being the a axis unmodified within the experimental uncertainties. It is worth to note that [100], which corresponds to the axial direction of the borate chains (Figure 1), was also found to be the less compressible axis at high pressure conditions (Lotti et al. 2017).

14

3.5 Crystal-structure modifications with decreasing temperature

The main effect of the $P2_1/a$-to-$P2_1$ phase transition in colemanite is the loss of the glide plane a, and of the related inversion center, which allows the transition to the ferroelectric state. The loss of the glide plane gives rise to a change of the symmetry constraints among the neighboring H_2O molecules, which are symmetry-independent in the $P2_1$ polymorph (Figure 2). According to Hainsworth and Petch (1966), this leads to a static ordering of the H5 and H2 hydrogen atoms all over the crystal volume: i.e., with H51 ordered in the A configuration (bridging H-bond between the H_2O molecules) and H52 ordered in the B configuration, or *vice versa*. In order to check the validity of this model, we calculated the difference-Fourier maps of the electron density, based on the X-ray diffraction data collected between 260 and 104 K, and the difference-Fourier maps of the nuclear density, based on neutron diffraction data collected at 20 K (Figure 6). In any calculated map, the residual peaks of the electron and nuclear densities (based on H-free structure refinements) suggested the persistence of the A and B configurations for both the symmetry-independent H51 and H52 sites (Figure 6). These results can be in agreement with the model proposed by Hainsworth and Petch (1966) if we assume the distribution over the crystal volume of two different domains, each of them showing an opposite internal order.

The structure refinements based on the X-ray diffraction data collected at different temperatures allow a comparative analysis of the T-induced structural modifications. The in situ high-pressure study (Lotti et al. 2017) showed that the hydrostatic compression in colemanite is mainly accommodated by tilting of the cations polyhedra around the shared oxygen atoms and by the compression of the Ca-polyhedron. Following the same protocol adopted by Lotti et al. (2017), the volumes of the B and Ca coordination polyhedra have been calculated using the tools implemented in the software *Vesta* (Momma and Izumi 2011). The calculated values are reported in Table 3 and show that no significant changes occur to the B tetrahedra at decreasing temperature and only a minor shrinkage affects the Ca-polyhedra. Therefore, in contrast to the high-P behavior, the

15

354 (moderate) volume contraction induced by the *T*-decrease is mainly accommodated by a tilting

355 mechanism of the structural units, as this mechanism is energetically more favorable than distortion

356 or compression (Gatta 2010). It is worth to note that the unit-cell volume shrinking at 104 K (0.9

357 %), according to the isothermal equation of state reported by Lotti et al. (2017), is equivalent (in

358 magnitude) to the bulk compression observed at 0.66 GPa.

359 The loss of the glide plane due to the phase transition to the $P2_1$ space group induces the split of

360 every atomic site in two independent positions. The loss of the symmetry constraints allows the

361 displacement, from the previous centrosymmetric configuration, of any couple of atoms with a

362 common parent site. This displacement allows an asymmetrical distribution of charged ions along

363 the *b* axis, which was proposed to be the source for the ferro-, pyro- and piezo-electric behavior of

364 colemanite below the transition temperature (Hainsworth and Petch 1966). This displacement has

365 been modeled for any couple of atoms as the virtual interatomic distance (along [010]) in the $P2_1/a$

366 space group (Figure 5 and Table S8). Figure 5 shows that, for the heavier Ca, B and O couples of

367 atoms, the average displacement from the centrosymmetric configuration increases in the range

368 between 260 and 180 K and is substantially constant in the range between 180 and 104 K. A similar

369 behavior was reported for the spontaneous polarization of colemanite below the transition

370 temperature (Wieder 1959; Wieder et al. 1962).

371

372 **4. Conclusions**

373 • The crystal chemistry and the low-temperature behavior of natural colemanite, a hydrous

374   Ca-borate of high economic relevance, were investigated by means of a multi-

375   methodological approach.

376 • The composition of the major and of more than fifty potential trace elements has been, to the

377   best of our knowledge for the first time, thoroughly investigated adopting different

378   analytical techniques, representing a unique experimental approach in the crystal chemistry

379   of borate minerals.

380   • The displacive phase transition from the $P2_1/a$ space group to the ferroelectric $P2_1$ subgroup

381   was found to occur between 261 and 275 K with a peak at 270.5 K.

382   • The structure refinements of the $P2_1$-colemanite, based on in situ low-T X-ray and neutron

383   diffraction data, suggest that the distribution of the proton sites (belonging to H_2O

384   molecules) is still disordered.

385   • The comparative elastic and structural analyses at varying temperature showed that the

386   borate chains direction (i.e., the a axis) is almost unaffected by the temperature variation and

387   that the asymmetric distribution of ionic charges along the b crystallographic axis, following

388   the phase transition, is likely responsible for the reported ferro-, pyro- and piezo-electric

389   behavior of the $P2_1$-colemanite.

390

395

6. References

Burns PC, Hawthorne FC (1993) Hydrogen bonding in colemanite: an X-ray and structure-energy study. Can Mineral 31:297-304.

Christ CL, Clark JR, Evans HT (1954) The stucture of colemanite, $CaB_3O_4(OH)_3 \cdot H_2O$, determined by the direct method of Hauptman and Karle. Acta Cryst 7:453-454.

Christ CL, Clark JR, Evans HT (1958) Studies of Borate Minerals (III): The Crystal Structure of Colemanite, $CaB_3O_4(OH)_3 \cdot H_2O$. Acta Cryst 11:761-770.

Chynoweth AG (1957) The Pyroelectric Behaviour of Colemanite. Acta Cryst 10:511-514.

Clark JR, Appleman DE, Christ CL (1964) Crystal chemistry and structure refinement of five hydrated calcium borates. J Inorg Nucl Chem 26:73-95.

Coppens P, Leiserowitz L, Rabinovich D (1965) Calculation of absorption corrections for camera and diffractometer data. Acta Cryst 18:1035-1038.

Crangle RD (2015) Boron. In: US Geological Survey (ed) Minerals Yearbook: Volume I - Metals and Minerals. US Geological Survey, Reston, pp 13.1-13.8.

Fenzl W, Schuppler S (1994) Thermal-wave investigation of the ferroelectric phase transition in colemanite. Z Phys B 93:343-348.

Garrett DE (1998) Borates. Handbook of Deposits, Processing, Properties and Use. Academic Press, Cambridge.

Gatta GD (2010) Extreme deformation mechanisms in open-framework silicates at high-pressure: Evidence of anomalous inter-tetrahedral angles. Micropor Mesopor Mater 128:78–84.

416   Gatta GD, Rotiroti N, Fisch M, Armbruster T (2010a) Stability at high pressure, elastic behavior

417   and pressure-induced structural evolution of "Al_5BO_9", a mullite-type ceramic material. Phys

418   Chem Minerals 37:227-236.

419   Gatta GD, Vignola P, McIntyre GJ, Diella V (2010b) On the crystal-chemistry of londonite

420   [(Cs,K,Rb)$Al_4Be_5B_{11}O_{28}$]: a single-crystal neutron diffraction study at 300 and 20 K. Am

421   Mineral 95:1467-1472.

422   Gatta GD, Vignola P, Lee Y (2011) Stability of (Cs,K)$Al_4Be_5B_{11}O_{28}$ (londonite) at high

423   pressure and high temperature: a potential neutron absorber material. Phys Chem Minerals

424   38:429-434.

425   Gatta GD, Lotti P, Merlini M, Liermann H-P, Fisch M (2013) High-pressure behavior and phase

426   stability of Al_5BO_9, a mullite-type ceramic material. J Am Cer Soc 96:2583-2592.

427   Gatta GD, Lotti P, Comboni D, Merlini M, Vignola P, Liermann H-P (2017) High-pressure

428   behaviour of (Cs,K)$Al_4Be_5B_{11}O_{28}$ (londonite): a single-crystal synchrotron diffraction study up

429   to 26 GPa. J Am Cer Soc, in press. doi: 10.1111/jace.14936.

430   Gavrilova ND, Lotonov AM, Antonenko AA (2006) Ferroelectric Properties of Colemanite.

431   Inorg Mater 42:777-781.

432   Giron D (1995) Thermal analysis and calorimetric methods in the characterization of

433   polymorphs and solvates. Thermochimica Acta 248:1-59

434   Gonzalez-Platas J, Alvaro M, Nestola F, Angel R (2016) EosFit7-GUI: a new graphical user

435   interface for equation of state calculations, analyses and teaching. J Appl Crystallogr 49:1377-

436   1382.

437   Hainsworth FN, Petch HE (1966) The structural basis of ferroelectricity in colemanite. Can J

438   Phys 44:3083-3107.

439   Helvaci C (1995) Stratigraphy, Mineralogy, and Genesis of the Bigadiç Deposits, Western

440   Turkey. Econ Geol 90:1237-1260.

441   Helvaci C (2015) Geological features of neogene basins hosting borate deposits: on overview of

442   deposits and future forecasts, Turkey. Bull Min Res Exp 151:169-215.

443   Helvaci C, Alonso RN (2000) Borate Deposits of Turkey and Argentina; A Summary and

444   Geological Comparison. Turkish J Earth Sci 9:1-27.

445   Helvaci C, Öztürk YY, Emmermann A (2017) Fluorescence survey of Turkish borate minerals:

446   comparative measurements of fluorescence spectra of the most important borate mineral

447   species, Turkey. N Jb Miner Abh 194:1-17.

448   Holuj F, Petch HE (1960) A nuclear magnetic resonance study of colemanite. Can J Phys

449   38:515-546.

450   Howard JAK, Johnson O, Schultz AJ, Stringer AM (1987) Determination of the neutron

451   absorption cross section for hydrogen as a function of wavelength with a pulsed neutron source.

452   J Appl Crystallogr 20:120-122.

453   Kabsch W (2010) XDS. Acta Cryst D66:125-132.

454   Kawakami K (2007) Reversibility of enantiotropically related polymorphic transformations

455   from a practical viewpoint: Thermal analysis of kinetically reversible/irreversible polymorphic

456   transformations. J Pharm Sci 96:982-989

457   Lausi A, Polentarutti M, Onesti S, Plaisier JR, Busetto E, Bais G, Barba L, Cassetta A, Campi

458   G, Lamba D, Pifferi E, Mande SC, Sarma DD, Sharma SM, Paolucci G (2015) Status of the

459   crystallography beamlines at Elettra. Eur Phys J Plus 130:43.

460   Lehmann MS, Kuhs W, McIntyre GJ, Wilkinson C, Allibon J (1989) On the use of a small two-

461   dimensional position-sensitive detector in neutron diffraction. J Appl Crystallogr 22:562-568.

462   Lin J, Pan Y, Chen N, Mao M, Li R (2011) Arsenic incorporation in colemanite from borate

463   deposits: data from ICP-MS, μ-SXRF, XAFS and EPR analyses. Can Mineral 49:809-822.

464   Lotti P, Gatta GD, Comboni D, Guastella G, Merlini M, Guastoni A, Liermann H-P (2017)

465   High-pressure behavior and *P*-induced phase transition of $CaB_3O_4(OH)_3 \cdot H_2O$ (colemanite). J

466   Am Cer Soc 100:2209-2220.

467   Momma K, Izumi F (2011) Vesta 3 for three-dimensional visualization of crystal, volumetric

468   and morphology data. J Appl Crystallogr 44:1272-1276.

469   Perloff A, Block S (1960) Low temperature phase transition of colemanite. Am Mineral 45:229.

470   Petricek V, Dusak M, Palatinus L (2014) Crystallographic Computing System JANA2006:

471   General features. Z Kristallogr 229:345-352.

472   Slabkaya GL, Lotonov AM, Gavrilova ND (2004) Low-Frequency Dielectric Spectroscopy and

473   Electrical Properties of $Ca[B_3O_4(OH)_3] \cdot H_2O$ Single Crystals near the Phase Transition. Inorg

474   Mater 40:1489-1494.

475   US Geological Survey (2007) Mineral Commodity Summaries 2006. US Geological Survey,

476   Reston.

477   Wieder HH (1959) Ferroelectric Properties of Colemanite. J Appl Phys 30:1010-1018.

478   Wieder HH, Clawson AR, Parkerson CR (1962) Ferroelectric and Pyroelectric Properties of

479   Mineral and Synthetic Colemanite. J Appl Phys 33:1720-1725.

480   Wilkinson C, Khamis HW, Stansfield RFD, McIntyre GJ (1988) Integration of single-crystal

481   reflections using area multidetectors. J Appl Crystallogr 21:471-478.

482   Wilson AJC, Prince E (1999) International Tables for Crystallography. Volume C:

483   Mathematical, Physical and Chemical Tables, 2nd ed. Kluwer, Dordrecht.

484

Appendix I.

486   A thorough chemical analysis of the studied colemanite sample has been performed by adopting a

487   multi-methodological approach. In the following, a detailed description of the experimental

488   techniques, reported in section 2.2, is given.

489

490   **I.a Titrimetric determination of boron**

491   120-200 mg of the sample of colemanite were placed in a 50 ml plastic test tube. 5 ml of water and

492   3 ml of HCl 1M were added. The plastic test tube was then covered and transferred in an ultrasound

493   bath for 1-2 hours. The resulting clear solution was transferred in a 200-300 ml beaker with water

494   up to about 100 ml of total solution.

495   A combined glass electrode (InLab® Routine Pro – Mettler Toledo) was immersed in the solution

496   and the pH was adjusted to 5.5-6.5, by the addition of HCl 0.1-1M and NaOH 0.1-1M. 5-6 grams of

497   mannitol were added and stirred until complete dissolution. The resulting solution was titrated with

498   NaOH 0.1M up to pH = 8.3-8.7.

499   Due to the absence in the sample of hydrolyzing elements, as well as of elements able to influence

500   the acidity of the solution, it can be inferred that the titrated acid content is entirely due to the

501   presence of boric acid in solution. The results are reported in Table S1 (supplementary materials).

502

503   **I.b EDTA (Ethylenediaminetetraacetic acid) titrimetric method of Calcium**

504   40-80 mg of colemanite were placed in a 50 ml plastic test tube along with 5 ml of water and 1 ml

505   of HCl 1M. The plastic tube was subsequently covered with lid and transferred in an ultrasound

506   bath for 1-2 hours.

507   The resulting clear solution was transferred in a 300-400 ml beaker and diluted to 200 ml with

508   water. 10 ml of buffer solution (pH = 10 mixture of ammonium chloride/ammonia) and 3-4 drops of

509   Eriochrome black T solution (2gr/l in ethanol) were added. The solution was titrated with a standard

510   solution of EDTA 0.01 M [solution of EDTA with $5 \cdot 10^{-4}$ mol/l of magnesium chloride

511   exahydrate($MgCl_2 \cdot 6H_2O$)], until its purple color was altered to blue. The total volume of EDTA

512   added to the solution is proportional to the average content of Ca and Sr in the colemanite sample

513   (Table S2, supplementary material).

514

515   **I.c Determination of carbon and hydrogen by thermal decomposition and detection by**

516   **Infrared absorption (C,H).**

517   100-300 mg of the natural sample of colemanite were decomposed at 950°C in an elementary

518   analyzer LECO Truspec CHN, in excess of oxygen for 90 seconds. The products of decomposition

519   were passed through a second furnace (Afterburner) at 850°C for a further oxidation and particulate

520   removal. The gases, collected and homogenized in a container of 4.5 liters at 50°C, were sent to the

521   detectors for infrared absorption for the measurement of CO_2 and H_2O (i.e., carbon is measured in

522   the form of CO_2 and hydrogen in the form of H_2O).

523   EDTA, sodium tetraborate decahydrate (borax, $Na_2B_4O_7 \cdot 10H_2O$), boric acid (H_3BO_3), calcium

524   carbonate ($CaCO_3$), sodium nitrate ($NaNO_3$) and oxalic acid (dehydrated) ($HO_2CCO_2H \cdot 2H_2O$) were

525   used as calibration standards. The results are reported in Table S3 (supplementary material).

526

527   **I.d Determination of fluorine by Ion selective electrode**

528   5-20 mg of the colemanite sample were placed in a 50 ml plastic test tube along with 5 ml of water

529   and 3 ml of hydrochloric acid 1M. The plastic test tube was covered and transferred in an

530   ultrasound bath for 1-2 hours. Later, 2-3 ml of Total Ionic Strength Adjustment Buffer (Commercial

531   solution TISAB III) were added to the solution and diluted to 20 ml with water. The content of

532   fluorine was determined using a *perfectION™ Combination Fluoride Ion Selective Electrode* (from

533   Mettler Toledo) adopting the standard addition method of certified reference material solution of F

534   from 0.1 to 2 mg/l (Table S4, supplementary material).

535

536   <mark>I.e</mark> Determination of minor elements by ICP-AES

537   All the measurements were performed in radial view mode with an ICP/AES Perkin Elmer Optima

538   7000DV spectrometer. For the rare earth elements, 5-20 mg of colemanite sample were placed in a

539   50 ml plastic test tube along with 5 ml of water and 3 ml of hydrochloric acid 1M. The plastic test

540   tube was covered and transferred in an ultrasound bath for 1-2 hours. The solution was transferred

541   and diluted with water in a 25 ml volumetric flask. A blank solution and series solution for

542   calibrations were prepared carrying out the same procedure without the sample. A certified

543   reference material (CRM) multi-elemental standard mix for ICP (50mg/l) of each element was used

544   for preparing the solution series for calibration (5 solutions from 0,05 mg/l to 1 mg/l for each

545   element).

546   For the analysis of the other elements investigated by ICP-AES (Table S5, supplementary material),

547   the decomposition of the colemanite sample was obtained by alkaline fusion of 5-20 mg in a

548   platinum crucible with 100 mg of Na_2CO_3 or K_2CO_3 in a muffle furnace at 1000°C for 5 minutes,

549   followed by dissolution in 10 ml of water and 1 ml of H_2SO_4 1M or 1 ml of HCl 1M. The resulting

550   clear solution was transferred and diluted with water in a 25 ml volumetric flask containing 2.5 ml

551   of Sc solution (100 mg/l) as internal standard.

552

553   <mark>I.f</mark> Determination of chloride, bromide, iodide by ion-chromatography

554   25 mg of the colemanite sample were placed in a 50 ml plastic test tube along with 20 ml of water

555   and one drop of nitric acid. The plastic test tube was covered and transferred in an ultrasound bath

556   for 1-2 hours. The solution was transferred and diluted with water in a 25 ml volumetric flask. A

557   blank solution and series solutions for calibrations were made carrying out the same procedure

558   without the sample. CRM containing 100 mg/l of each element was used for preparing the solution

559   series for calibration (5 solutions from 0,1 mg/l to 2 mg/l for each element). The analysis was

560   performed using a *Dionex ICS-1600 Standard Integrated IC* system equipped with *Columns ION*

561   *PACK AG23 Guard 4x50 mm + AS23 4x250mm*. A solution of KOH 10mM was used as eluent. The

562   results are reported in Table S6 (supplementary material).

563

564   **I.g Determination of water content by heating**

565   500-600 mg of the colemanite sample were placed in a quartz crucible with lid and gradually heated

566   in a muffle furnace from ambient temperature up to 800°C. Between 300 and 400°C, the sample

567   was partially lost during heating, the weight loss being due to H_2O and partially to inorganic matter.

568   B, Ca and Sr were analyzed in the residual sample in order to provide suitable corrections. The

569   results are reported in Table S7 (supplementary material).

570

Figure 1. (*Top*) The structure of colemanite viewed down the [010] axis. The heteropolyhedral

sheet made by the B- and Ca-polyhedra chains is shown. (*Bottom*) The structure of colemanite

viewed down the [001] axis, showing the complex H-bonding network.
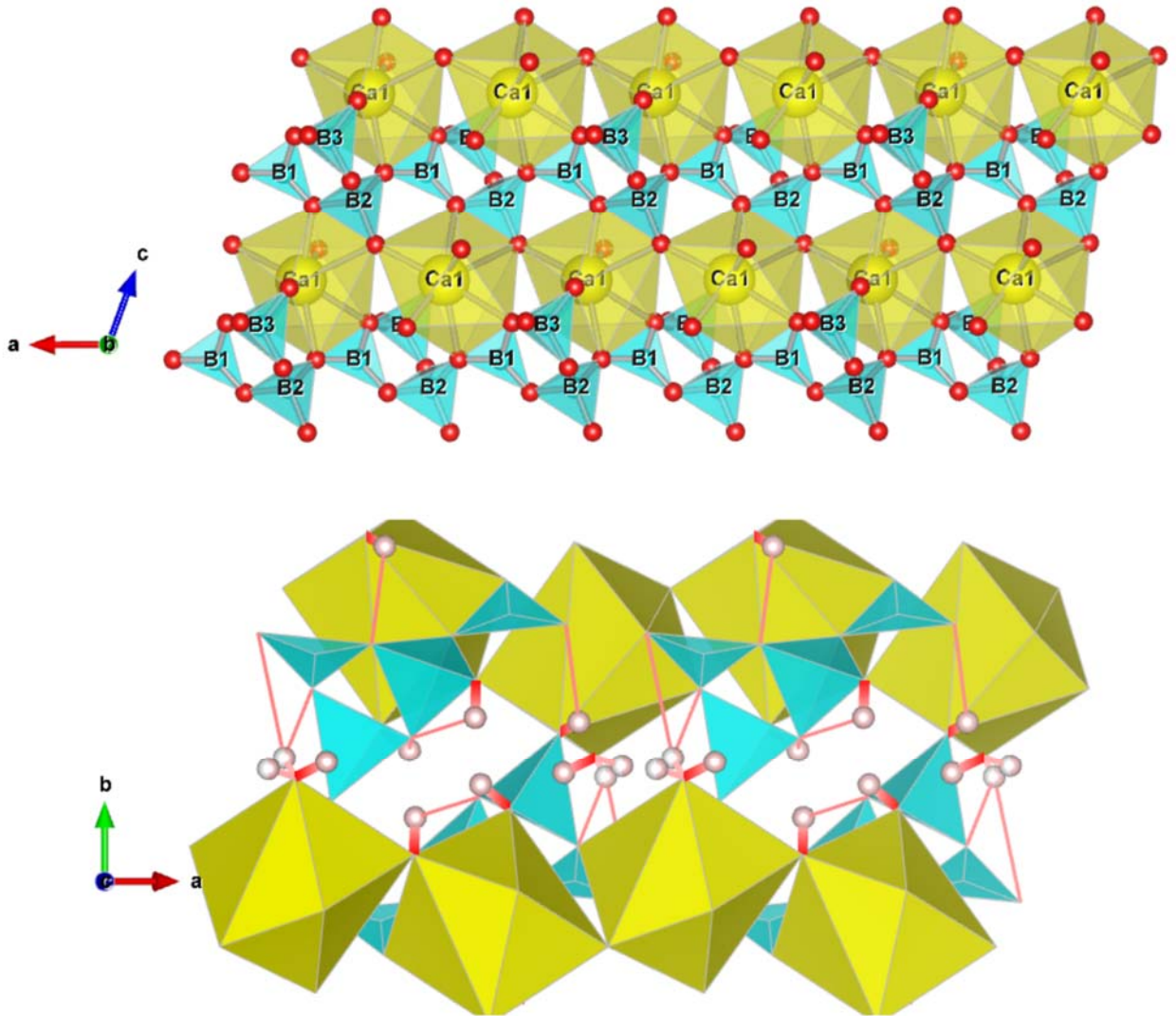
578   **Figure 2**. Bonding configuration of the H_2O molecules of: (*A and B*) $P2_1/a$-colemanite; (C) $P2_1$-

579   colemanite, according to the model proposed by Hainsworth and Petch (1966); (D.1 and D.2)

580     $P2_1$-colemanite, according to the structure refinement of this study, based on neutron diffraction

581   data collected at 20 K. Thick and thin lines represent ionic- and hydrogen-bonds, respectively.

582   Dashed lines represent mutually exclusive bonds. D.1 and D.2 represent two mutually exclusive

583   configurations.
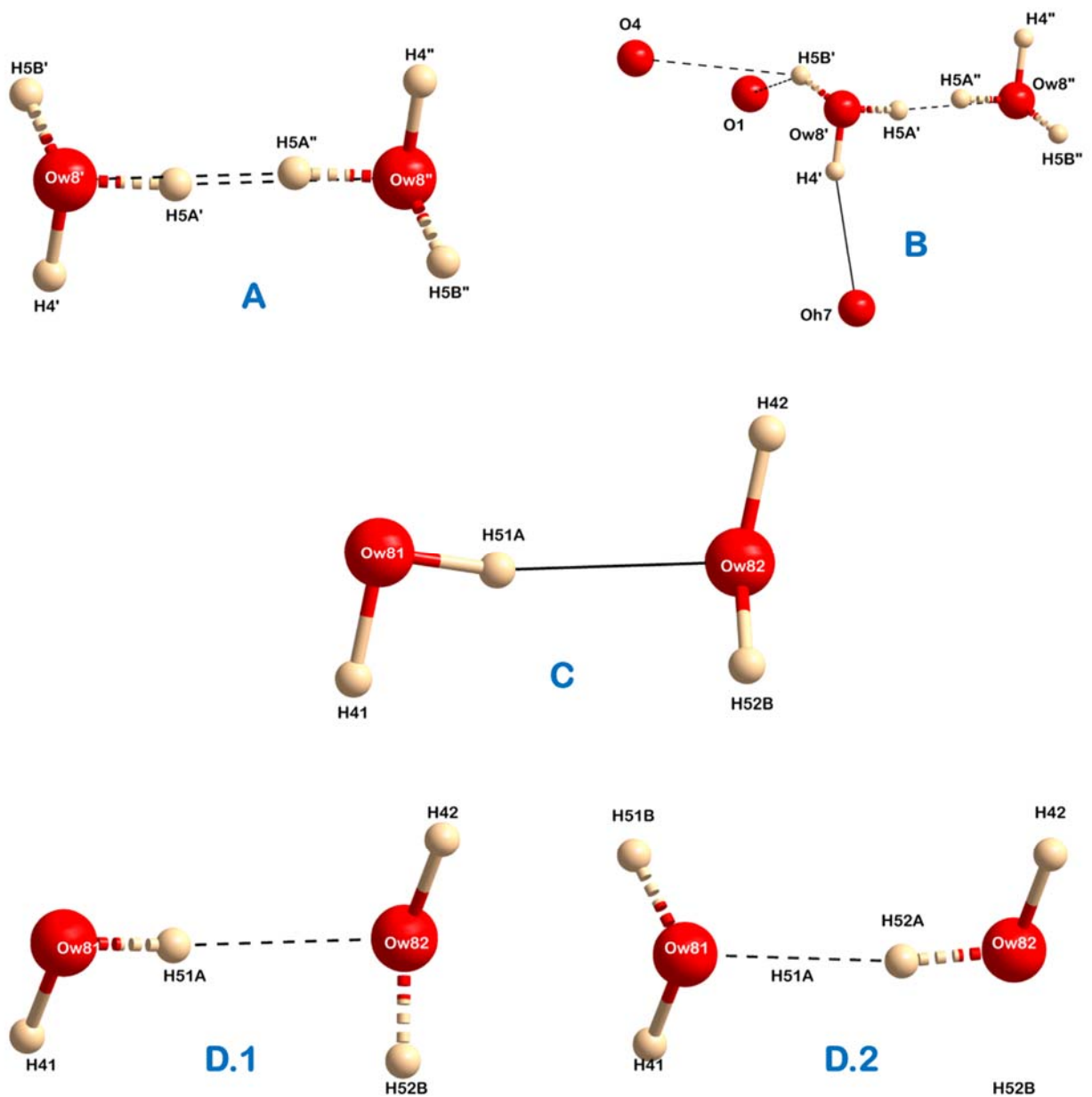
584
585

586 **Figure 3.** Excerpts from the differential scanning calorimetry (DSC) curve of the colemanite
587 sample showing: A) the endothermic peak observed in the first heating cycle; B) the exothermic
588 peak observed in the cooling cycle and C) the endothermic peak observed in the second heating
589 cycle. No hysteresis phenomena can be detected. An estimate of the calorimetric enthalpy
590 obtained by integration of the transition peaks is reported. The full spectrum of the experimental
591 DSC curve is reported in Figure 1S (supplementary materials).

Integral   -1.8 mJ
Normalized   -0.29 J/g
Onset   -13.33°C
Peak   -2,53°C
Endset   -0.79°C

Lab: Hermes   STAR° SW 10.00

Integral   1.52 mJ
Normalized   0.24 J/g
Onset   0.76°C
Peak   -2,31°C
Endset   -10.82°C

Integral   -2.35 mJ
Normalized   -0.37 J/g
Onset   -12.53°C
Peak   -2,53°C
Endset   -0.72°C

Lab: Hermes   STAR° SW 10.00
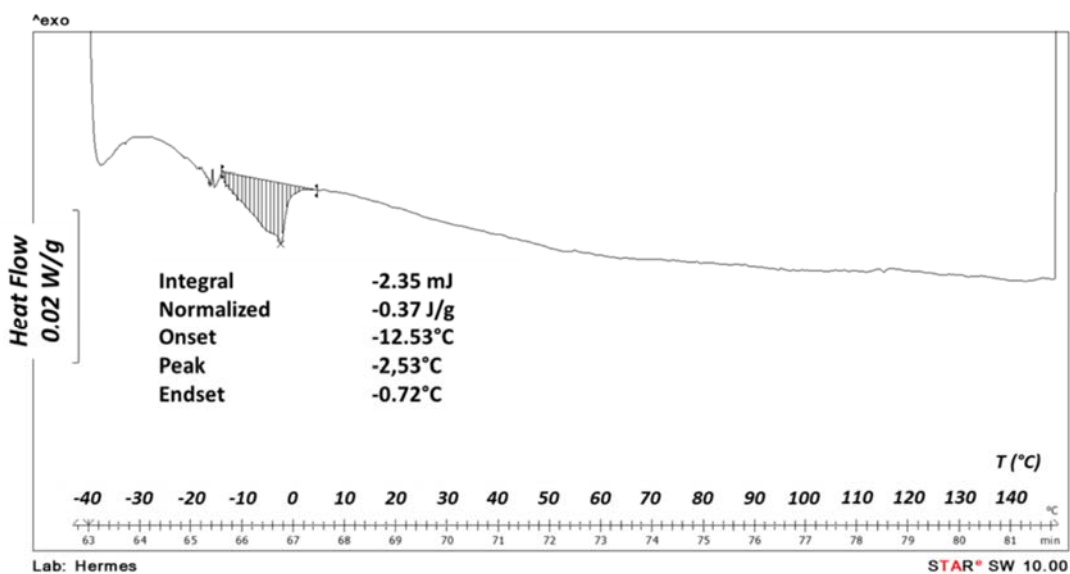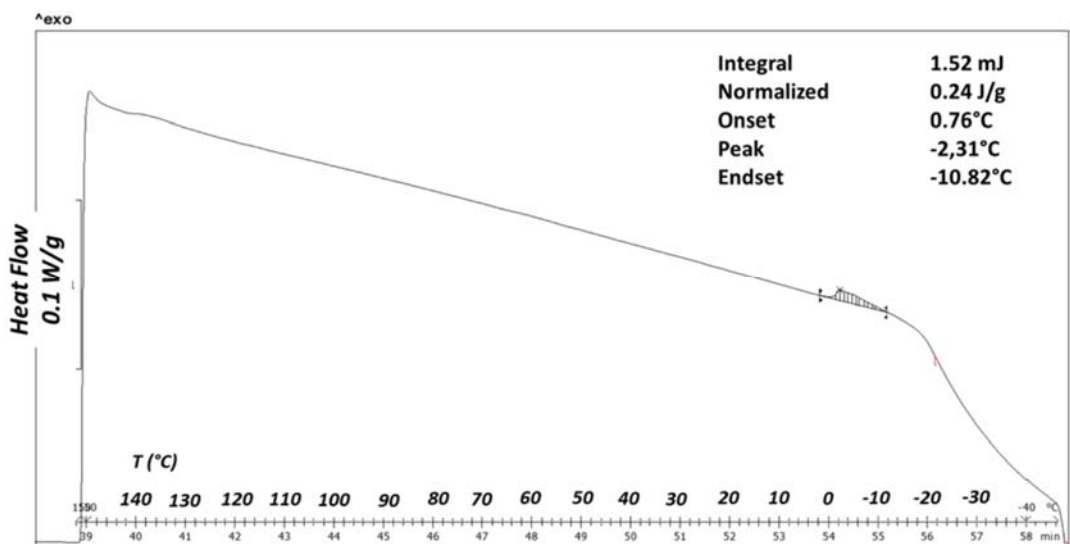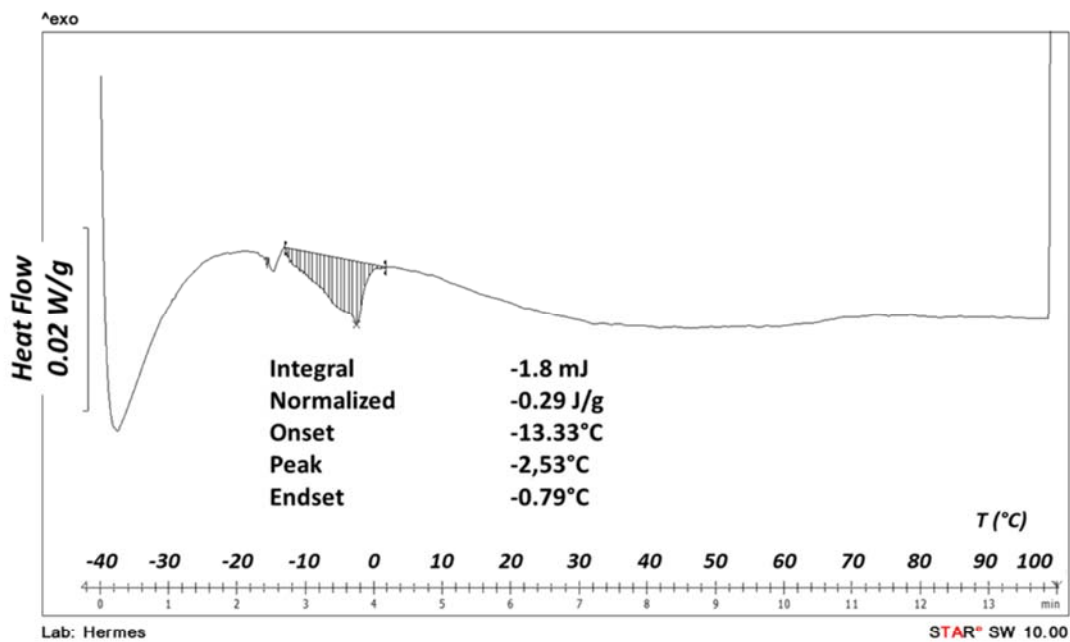
Figure 4. Reconstruction of the $h0l*$ reciprocal lattice planes, based on the X-ray diffraction data

collected at 300 K (*left*) and 104 K (*right*), respectively. The diffraction peaks violating the

extinction condition for $h = 2n +1$ are encircled.
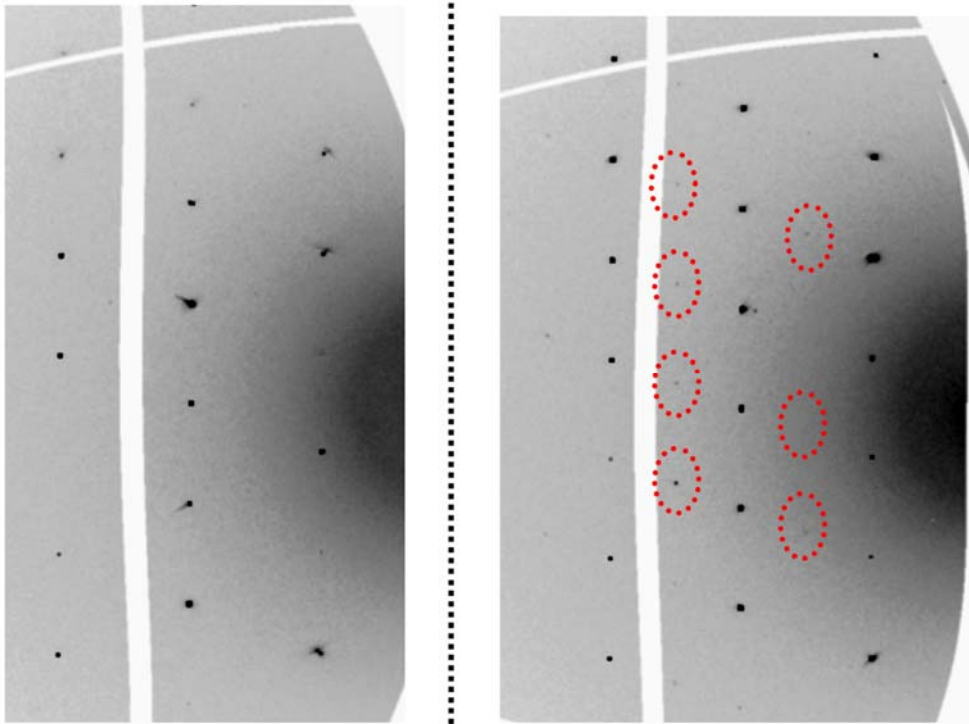
Figure 5. (*Top*). Evolution of the unit-cell parameters of colemanite with *T*, normalized to their
values at 300 K. (*Bottom*). Calculated displacement along the **b**-axis, with respect to the
centrosymmetric configuration, of selected couples of atoms of $P2_1$-colemanite, sharing a
common parent site in the $P2_1/a$ space group (see section 3.5 for further details).
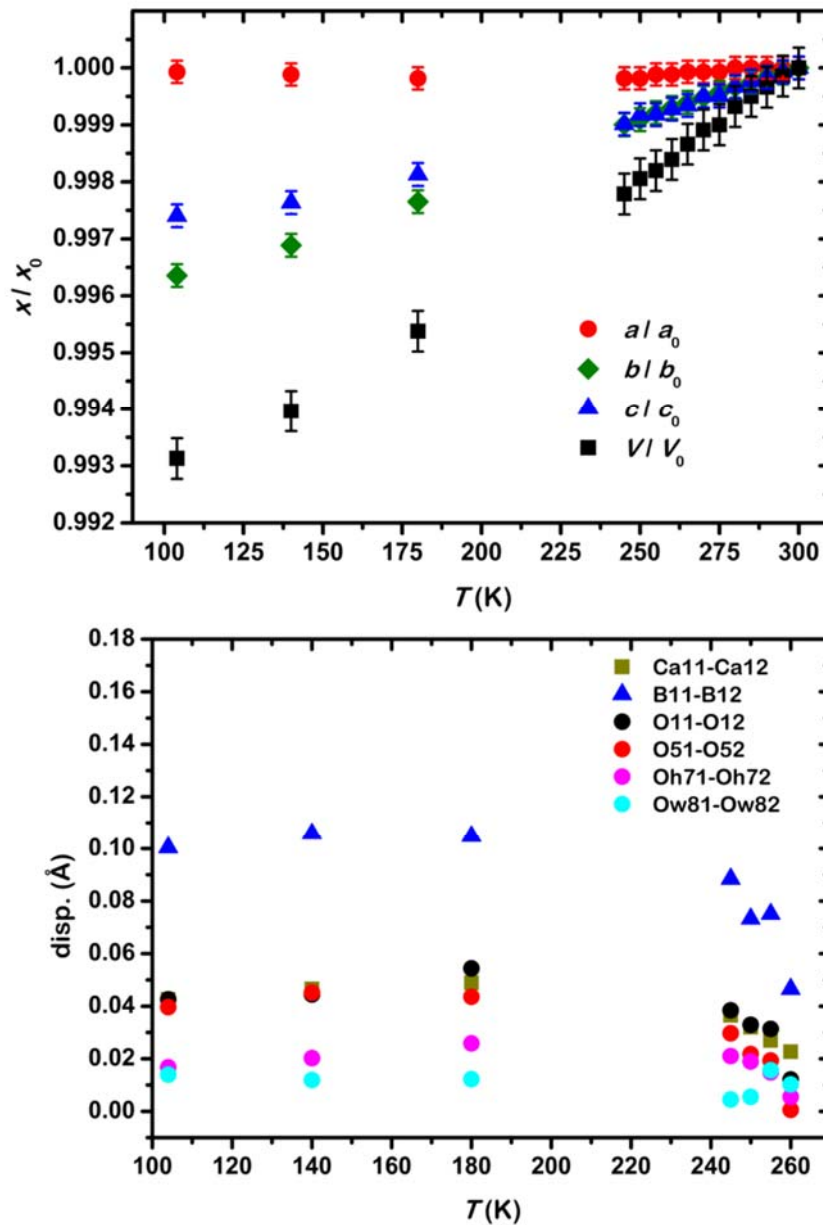
Figure 6. Difference-Fourier map of the nuclear density in the proximity of the H_2O molecules, based on H-free neutron structure refinements at 20 K. The negative residues related to the H positions are shown. The yellow surfaces represent the isosurface at -1.5 fm/Å³. For a sake of clarity, the positive residues are not shown. The red spheres represent the H_2O-oxygen sites.
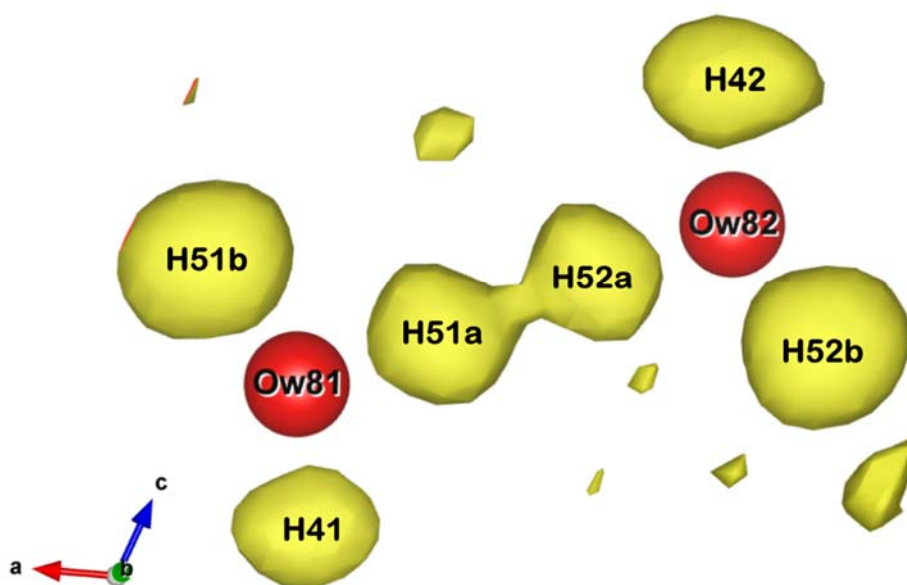
609   **Table 1.** The mass fractions of the main chemical components of the sample of colemanite here
610   investigated, measured by means of a multi-methodological approach. Further details are in the text
611   (sections 2.2, 3.1 and Appendix I) and in Tables S1-S7 (supplementary materials).

612

	wt%
B_2O_3	50.8(4)
CaO	27.2(2)
SrO	0.30(5)
SiO_2	0.03(1)
H_2O	21.8(4)

613 **Table 2**. Unit-cell parameters of colemanite and details of the structure refinements at different temperatures.

T (K)	300	295	290	285	280	275	270	265	260	255	250
Space group	$P2_1/a$	$P2_1/a$	$P2_1/a$	$P2_1/a$	$P2_1/a$	$P2_1/a$	$P2_1/a$	$P2_1/a$	$P2_1$	$P2_1$	$P2_1$
a (Å)	8.714(2)	8.714(2)	8.714(2)	8.714(2)	8.714(2)	8.713(2)	8.713(2)	8.713(2)	8.713(2)	8.713(2)	8.712(2)
b (Å)	11.244(2)	11.243(2)	11.242(2)	11.241(2)	11.240(2)	11.239(2)	11.238(2)	11.237(2)	11.236(2)	11.235(2)	11.234(2)
c (Å)	6.0904(10)	6.0900(10)	6.0894(10)	6.0894(10)	6.0884(10)	6.0874(10)	6.0874(10)	6.0864(10)	6.0860(10)	6.0854(10)	6.0854(10)
β (°)	110.12(3)	110.12(3)	110.12(3)	110.12(3)	110.12(3)	110.12(3)	110.12(3)	110.12(3)	110.13(3)	110.13(3)	110.13(3)
V (Å^3)	560.3(2)	560.2(2)	560.1(2)	560.0(2)	559.9(2)	559.8(2)	559.7(2)	559.6(2)	559.4(2)	559.3(2)	559.2(2)
min $\leq h,k,l \leq$ max	$0 \leq h \leq 12$ $-16 \leq k \leq 0$ $-8 \leq l \leq 8$	$0 \leq h \leq 12$ $-16 \leq k \leq 0$ $-8 \leq l \leq 8$	$0 \leq h \leq 12$ $-16 \leq k \leq 0$ $-8 \leq l \leq 8$	$0 \leq h \leq 12$ $-16 \leq k \leq 0$ $-8 \leq l \leq 8$	$0 \leq h \leq 12$ $-16 \leq k \leq 0$ $-8 \leq l \leq 8$	$0 \leq h \leq 12$ $-16 \leq k \leq 0$ $-8 \leq l \leq 8$	$0 \leq h \leq 12$ $-16 \leq k \leq 0$ $-8 \leq l \leq 8$	$0 \leq h \leq 12$ $-16 \leq k \leq 0$ $-8 \leq l \leq 8$	$0 \leq h \leq 12$ $-16 \leq k \leq 0$ $-8 \leq l \leq 8$	$0 \leq h \leq 12$ $-16 \leq k \leq 0$ $-8 \leq l \leq 8$	$0 \leq h \leq 12$ $-16 \leq k \leq 0$ $-8 \leq l \leq 8$
Unique peaks	1695	1700	1693	1691	1706	1696	1695	1708	1785	1787	1784
Observed peaks $F_o^2/\sigma(F_o^2)>3$	1675	1679	1670	1667	1686	1675	1678	1686	1718	1739	1740
R_{int} (obs)	0.0361	0.0355	0.0355	0.0357	0.0379	0.0352	0.0369	0.0376	0.0383	0.0384	0.0402
R_{int} (all)	0.0361	0.0355	0.0355	0.0357	0.0379	0.0352	0.0369	0.0376	0.0383	0.0384	0.0402
Refined param.	129	129	129	129	129	129	129	129	205*	215	215
R_1 (obs)	0.0242	0.0236	0.0224	0.0236	0.0257	0.0251	0.0228	0.0266	0.0307	0.0277	0.0268
R_1 (all)	0.0243	0.0237	0.0225	0.0238	0.0258	0.0252	0.0229	0.0267	0.0318	0.0282	0.0273
wR_1 (obs)	0.0418	0.0405	0.0400	0.0417	0.0425	0.0424	0.0418	0.0433	0.0489	0.0442	0.0407
Residuals (e^-/Å^3)	+0.45 -0.45	+0.48 -0.53	+0.41 -0.44	+0.39 -0.45	+0.56 -0.70	+0.63 -0.65	+0.41 -0.57	+0.74 -0.69	+0.63 -0.66	+0.40 -0.72	+0.47 -0.73

* O11 and O12 displacement parameters refined as isotropic for the data collected at 260 K, see section 2.4 for further details

T (K)	245	180	140	104	20*
Space group	$P2_1$	$P2_1$	$P2_1$	$P2_1$	$P2_1$
a (Å)	8.712(2)	8.712(2)	8.713(2)	8.713(2)	8.711(5)
b (Å)	11.233(2)	11.218(2)	11.209(2)	11.203(2)	11.189(8)

c (Å)	6.0844(10)	6.0790(10)	6.0760(10)	6.0746(10)	6.071(4)
β (°)	110.13(3)	110.16(3)	110.19(3)	110.21(3)	110.3(2)
V (Å^3)	559.1(2)	557.7(2)	556.9(2)	556.5(2)	555(2)
min ≤ h,k,l ≤ max	$0 \le h \le 12$ $-16 \le k \le 0$ $-8 \le l \le 8$	$0 \le h \le 12$ $-16 \le k \le 0$ $-8 \le l \le 8$	$0 \le h \le 12$ $-16 \le k \le 0$ $-8 \le l \le 8$	$0 \le h \le 12$ $-16 \le k \le 0$ $-8 \le l \le 8$	$-12 \le h \le 7$ $-15 \le k \le 13$ $-7 \le l \le 8$
Unique peaks	1764	1776	1779	1784	1923
Observed peaks $F_o^2/\sigma(F_o^2) > 3$	1724	1747	1744	1755	1777
R_{int} (obs)	0.0344	0.0389	0.0330	0.0323	0.0501
R_{int} (all)	0.0344	0.0389	0.0330	0.0323	0.0507
Refined param.	215	215	215	215	117
R_1 (obs)	0.0218	0.0220	0.0214	0.0211	0.0905
R_1 (all)	0.0222	0.0223	0.0219	0.0214	0.0988
wR_1 (obs)	0.0367	0.0360	0.0396	0.0404	0.0987
Residuals (e^-/Å^3; fm/Å^3)	+0.38 -0.33	+0.36 -0.35	+0.38 -0.34	+0.39 -0.35	+4.60 -3.66

*neutron diffraction data

$R_{int} = \Sigma|F^2_{obs} - F^2_{obs(mean)}| / \Sigma(F^2_{obs})$; $R_1 = \Sigma(|F_{obs} - F_{calc}|)/\Sigma|F_{obs}|$;
$wR_1 = (\Sigma(w(F^2_{obs} - F^2_{calc})^2)/ \Sigma(w(F^2_{obs})^2)^{0.5})$, $w = 1/(\sigma^2(F^2_{obs}))$

Table 3. Average bond lengths (Å, triangularly coordinated boron) and volumes (Å^3) of the cations coordination polyhedra at different temperatures, based on the X-ray structure refinements.

T (K)	<B1-O> <B11-O>	<B12-O>	V(B2) V(B21)	V(B22)	V(B3) V(B31)	V(B32)	V(Ca) V(Ca11)	V(Ca12)	Residual voids*
300	1.3678(9)		1.638(1)		1.640(1)		26.142(8)		442.6(3)
295	1.3677(9)		1.639(1)		1.639(1)		26.140(7)		442.6(2)
290	1.3678(9)		1.639(1)		1.639(1)		26.135(7)		442.5(2)
285	1.3678(9)		1.639(1)		1.639(1)		26.133(8)		442.4(3)
280	1.3679(9)		1.639(1)		1.639(1)		26.129(8)		442.3(3)
275	1.3678(9)		1.638(1)		1.639(1)		26.123(8)		442.2(3)
270	1.3682(9)		1.638(1)		1.639(1)		26.121(7)		442.1(2)
265	1.368(1)		1.638(1)		1.639(1)		26.118(8)		442.0(3)
260	1368(3)	1.369(3)	1.641(3)	1.643(4)	1.638(3)	1.654(3)	26.10(2)	26.11(2)	441.9(3)
255	1.366(3)	1.369(3)	1.636(3)	1.641(3)	1.634(3)	1.644(3)	26.07(2)	26.16(2)	441.7(3)
250	1.366(3)	1.368(3)	1.637(2)	1.644(2)	1.632(2)	1.645(2)	26.06(2)	26.16(2)	441.7(3)
245	1.368(3)	1.367(3)	1.640(2)	1.640(3)	1.636(2)	1.642(2)	26.07(2)	26.15(2)	441.5(3)
180	1.369(3)	1.368(3)	1.638(2)	1.641(2)	1.639(2)	1.642(3)	25.99(2)	26.12(2)	440.4(3)
140	1.369(3)	1.368(3)	1.645(2)	1.635(2)	1.637(2)	1.643(3)	25.92(2)	26.14(2)	439.7(3)
104	1.369(3)	1.368(3)	1.643(2)	1.637(2)	1.634(2)	1.647(2)	25.8888	26.15(2)	439.3(3)

* defined as R.V. = $V_{\text{unit-cell}} - \Sigma_{\text{unit cell}}[V(\text{B}) + V(\text{Ca})]$

Table 4. Atomic coordinates, site occupancy factors (fixed) and isotropic/equivalent displacement parameters ($Å^2$) from the structure refinements based on the X-ray diffraction data collected at 300 (space group $P2_1/a$) and 104 K (space group $P2_1$), respectively, and on the neutron diffraction data collected at 20 K (space group $P2_1$).

$P2_1/a$-colemanite at 300 K

Site	s.o.f.	x	y	z	$U_{iso/eq}$
Ca	1	0.63476(2)	0.21111(1)	0.73665(2)	0.0082(1)
B1	1	0.3344(1)	0.21262(6)	0.3139(1)	0.0057(2)
B2	1	0.03969(9)	0.17114(6)	0.1622(1)	0.0049(2)
B3	1	0.2206(1)	0.05222(7)	0.4962(1)	0.0053(2)
O1	1	-0.01827(6)	0.24681(5)	0.31544(9)	0.0074(2)
O2	1	0.18867(6)	0.23154(5)	0.13902(9)	0.0066(2)
Oh3	1	-0.08002(6)	0.16395(5)	-0.07283(9)	0.0083(2)
O4	1	0.34211(7)	0.14801(5)	0.50994(9)	0.0093(2)
O5	1	0.08715(6)	0.05573(4)	0.27086(8)	0.0058(2)
Oh6	1	0.29469(8)	-0.06590(5)	0.5144(1)	0.0114(2)
Oh7	1	0.16693(7)	0.07702(5)	0.69755(9)	0.0087(2)
Ow8	1	0.61366(8)	0.01897(6)	0.9010(1)	0.0164(2)
H1	1	-0.077(2)	0.094(1)	-0.128(3)	0.030(2)
H2	1	0.091(2)	0.033(1)	0.701(3)	0.030(2)
H3	1	0.345(2)	-0.086(1)	0.638(2)	0.030(2)
H4	1	0.695(2)	-0.010(1)	1.010(2)	0.030(2)
H5a	0.5	0.586(4)	-0.018(3)	0.770(3)	0.030(2)
H5b	0.5	0.544(4)	0.003(3)	0.972(6)	0.030(2)

$P2_1$-colemanite at 104 K

Site	s.o.f.	x	y	z	$U_{iso/eq}$
Ca11	1	0.88407(4)	0.21247(3)	0.73771(5)	0.0036(1)
Ca12	1	-0.38444(4)	-0.20863(4)	-0.73580(5)	0.0033(1)
B11	1	0.5843(2)	0.2082(2)	0.3135(3)	0.0026(3)
B12	1	-0.0839(2)	-0.2172(2)	-0.3160(3)	0.0038(3)
B21	1	0.2895(2)	0.1693(2)	0.1623(3)	0.0023(3)
B22	1	0.2186(2)	-0.1725(2)	-0.1625(3)	0.0032(3)
B31	1	0.4709(2)	0.0500(2)	0.4998(3)	0.0015(3)

B32	1	0.0211(3)	-0.0530(2)	-0.4958(3)	0.0036(3)
O11	1	0.2394(1)	0.2445(1)	0.3158(2)	0.0037(3)
O12	1	0.2676(1)	-0.2484(1)	-0.3175(2)	0.0037(3)
O21	1	0.4384(1)	0.2309(1)	0.1399(2)	0.0032(3)
O22	1	0.0678(1)	-0.2327(1)	-0.1383(2)	0.0035(3)
Oh31	1	0.1617(2)	0.1626(1)	-0.0729(2)	0.0045(3)
Oh32	1	0.3306(2)	-0.1648(1)	0.0725(2)	0.0036(4)
O41	1	0.5931(2)	0.1449(1)	0.5104(2)	0.0043(3)
O42	1	-0.0916(2)	-0.1504(1)	-0.5124(2)	0.0045(3)
O51	1	0.3381(1)	0.0533(1)	0.2707(2)	0.0024(2)
O52	1	0.1665(1)	-0.0566(1)	-0.2732(2)	0.0033(2)
Oh61	1	0.5445(2)	-0.0684(1)	0.5224(2)	0.0054(4)
Oh62	1	-0.0466(2)	0.0650(1)	-0.5101(2)	0.0060(4)
Oh71	1	0.4150(2)	0.0773(1)	0.6969(2)	0.0038(3)
Oh72	1	0.0888(2)	-0.0760(1)	-0.7025(2)	0.0054(4)
Ow81	1	0.8588(2)	0.0181(1)	0.9004(2)	0.0081(4)
Ow82	1	-0.3664(2)	-0.0170(1)	-0.8999(2)	0.0085(4)
H11	1	0.188(4)	0.091(2)	-0.121(6)	0.027(2)
H12	1	0.327(4)	-0.097(2)	0.131(6)	0.027(2)
H21	1	-0.060(4)	0.110(3)	-0.622(4)	0.027(2)
H22	1	0.615(3)	-0.085(3)	0.652(3)	0.027(2)
H31	1	0.337(3)	0.035(3)	0.697(5)	0.027(2)
H32	1	0.157(3)	-0.031(3)	-0.715(5)	0.027(2)
H41	1	0.930(3)	-0.018(4)	1.002(6)	0.027(2)
H42	1	-0.455(3)	0.008(5)	-1.008(5)	0.027(2)
H51a	0.5	0.773(5)	0.007(8)	0.94(1)	0.027(2)
H51b	0.5	0.844(5)	-0.026(4)	0.783(5)	0.027(2)
H52a	0.5	-0.302(6)	-0.005(8)	-0.978(8)	0.027(2)
H52b	0.5	-0.300(5)	0.026(4)	-0.779(6)	0.027(2)
$P2_1$-colemanite at 20 K					
Ca11	1	0.8821(9)	0.2081(6)	0.734(1)	0.0031(5)
Ca12	1	-0.3857(9)	-0.2131(6)	-0.741(1)	0.0031(5)

39

B11	1	0.5809(8)	0.2140(5)	0.314(1)	0.0023(3)
B12	1	-0.0878(8)	-0.2114(5)	-0.316(1)	0.0023(3)
B21	1	0.2901(7)	0.1679(5)	0.165(1)	0.0023(3)
B22	1	0.2191(7)	-0.1739(5)	-0.161(1)	0.0023(3)
B31	1	0.4725(7)	0.0522(6)	0.496(1)	0.0023(3)
B32	1	0.0399(7)	-0.0521(6)	-0.501(1)	0.0023(3)
O11	1	0.2394(7)	0.2460(5)	0.315(1)	0.0040(3)
O12	1	0.2675(7)	-0.2467(5)	-0.318(1)	0.0040(3)
O21	1	0.4363(7)	0.2314(5)	0.141(1)	0.0040(3)
O22	1	0.0696(8)	-0.2327(5)	-0.139(1)	0.0040(3)
Oh31	1	0.1602(7)	0.1572(4)	-0.077(1)	0.0040(3)
Oh32	1	0.3315(7)	-0.1691(4)	0.069(1)	0.0040(3)
O41	1	0.5926(7)	0.1504(5)	0.515(1)	0.0040(3)
O42	1	-0.0926(7)	-0.1460(5)	-0.509(1)	0.0040(3)
O51	1	0.3405(7)	0.0537(5)	0.273(1)	0.0040(3)
O52	1	0.1635(7)	-0.0561(5)	-0.272(1)	0.0040(3)
Oh61	1	0.5440(7)	-0.0669(5)	0.5077(9)	0.0040(3)
Oh62	1	-0.0469(8)	0.0668(6)	-0.5278(9)	0.0040(3)
Oh71	1	0.4199(7)	0.0718(5)	0.7063(9)	0.0040(3)
Oh72	1	0.0820(7)	-0.0805(5)	-0.6930(9)	0.0040(3)
Ow81	1	0.8637(7)	0.0138(6)	0.901(1)	0.0040(3)
Ow82	1	-0.3628(7)	-0.0188(5)	-0.901(1)	0.0040(3)
H11	1	0.179(1)	0.0777(7)	-0.142(2)	0.0185(5)
H12	1	0.335(1)	-0.0974(8)	0.125(2)	0.0185(5)
H21	1	-0.069(1)	0.0999(8)	-0.673(2)	0.0185(5)
H22	1	0.628(1)	-0.0812(8)	0.651(2)	0.0185(5)
H31	1	0.332(1)	0.021(1)	0.706(2)	0.0185(5)
H32	1	0.190(1)	-0.030(1)	-0.692(2)	0.0185(5)
H41	1	0.955(2)	-0.021(2)	1.020(3)	0.0185(5)
H42	1	-0.450(2)	0.021(1)	-1.016(3)	0.0185(5)
H51a	0.5	0.770(2)	0.0046(19)	0.955(3)	0.0185(5)
H51b	0.5	0.7859(15)	-0.0133(11)	0.762(2)	0.0185(5)

40

H52a	0.5	0.706(2)	0.0050(19)	1.024(3)	0.0185(5)
H52b	0.5	-0.3352(15)	0.0283(10)	-0.767(2)	0.0185(5)

Table 5. Hydrogen-bonding network as determined from the structure refinements based on the X-ray diffraction data collected at 300 and 104 K, respectively, and on the neutron diffraction data collected at 20 K.

T (K)		O_{donor}	H	$O_{acceptor}$	O_d-H (Å)	H···O_a (Å)	O_d-H-O_a (°)
300		Oh3	H1	O5	0.86(1)	1.89(1)	175(1)
104		Oh31	H11	O52	0.88(3)	1.87(2)	167(3)
		Oh32	H12	O51	0.85(3)	1.87(3)	175(3)
20		Oh31	H11	O52	0.97(1)	1.69(1)	176.1(8)
		Oh32	H12	O51	0.869(5)	1.905(6)	175.0(5)
300	*	Oh6	H2	O1	0.76(1)	2.37(2)	119(1)
	*	Oh6	H2	O2	0.76(1)	2.53(2)	130(1)
104	°	Oh61	H21	O11	0.83(2)	2.31(3)	119(3)
	°	Oh61	H21	O21	0.83(2)	2.54(3)	117(3)
	#	Oh62	H22	O12	0.81(3)	2.28(3)	121(3)
	#	Oh62	H22	O22	0.81(3)	2.30(3)	162(3)
20	°	Oh61	H21	O11	0.94(1)	2.26(1)	117.2(8)
	°	Oh61	H21	O21	0.94(1)	2.61(1)	110.9(8)
	#	Oh62	H22	O12	0.92(1)	2.43(1)	102.2(9)
	#	Oh62	H22	O22	0.92(1)	2.21(1)	143.9(9)
300		Oh7	H3	O5	0.83(2)	1.91(2)	174(2)
104		Oh71	H31	O52	0.83(3)	1.88(3)	174(3)
		Oh72	H32	O51	0.82(3)	1.90(3)	172(3)
20		Oh71	H31	O52	0.95(1)	1.73(1)	172(1)
		Oh72	H32	O51	0.98(1)	1.75(1)	172(1)
300		Ow8	H4	Oh7	0.85(1)	1.93(1)	164(2)
104		Ow81	H41	Oh72	0.86(3)	1.90(3)	160(4)
		Ow82	H42	Oh71	0.87(3)	1.92(3)	156(3)
20		Ow81	H41	Oh72	0.95(2)	1.85(2)	161(2)
		Ow82	H42	Oh71	0.95(2)	1.77(2)	160(2)
300	*	Ow8	H5a	Ow8	0.87(4)	1.81(4)	174(3)
	*	Ow8	H5b	O1	0.86(2)	2.72(3)	129(2)
	*	Ow8	H5b	O4	0.86(2)	2.48(3)	150(3)

104	°	Ow81	H51a	W82	0.87(5)	1.82(6)	165(5)
	°	Ow81	H51b	O11	0.84(4)	2.67(4)	135(3)
	°	Ow81	H51b	O42	0.84(4)	2.48(4)	135(3)
	#	Ow82	H52a	Ow81	0.86(6)	1.81(6)	171(4)
	#	Ow82	H52b	O12	0.87(3)	2.59(4)	137(3)
	#	Ow82	H52b	O41	0.87(3)	2.57(4)	130(3)
20	°	Ow81	H51a	W82	0.91(2)	1.77(2)	172(2)
	°	Ow81	H51b	O11	0.93(1)	2.73(1)	117.1(9)
	°	Ow81	H51b	O42	0.93(1)	2.69(2)	115(1)
	#	Ow82	H52a	Ow81	0.91(2)	1.78(2)	165(2)
	#	Ow82	H52b	O12	0.93(1)	2.60(1)	134(1)
	#	Ow82	H52b	O41	0.93(1)	2.43(2)	152(1)

*,°,#: mutually exclusive configurations

Table 6. Experimental X-ray diffraction peaks violating the extinction conditions expected for the $P2_1/a$ space group, at selected temperatures.

T (K)	Classes of reflections	$<I_{hkl}/\sigma(I_{hkl})>$	$I_{hkl}/\sigma(I_{hkl}) > 1.0$ *	$I_{hkl}/\sigma(I_{hkl}) > 3.0$ *	$I_{hkl}/\sigma(I_{hkl}) > 6.0$ *
300	$h00, h = 2n+1$	0.2	0	0	0
	$0k0, k = 2n+1$	0.2	1	0	0
	$h0l, h = 2n+1$	0.2	8	0	0
275	$h00, h = 2n+1$	0.2	0	0	0
	$0k0, k = 2n+1$	0.2	1	0	0
	$h0l, h = 2n+1$	0.3	10	0	0
270	$h00, h = 2n+1$	0.1	0	0	0
	$0k0, k = 2n+1$	0.2	0	0	0
	$h0l, h = 2n+1$	0.3	12	0	0
265	$h00, h = 2n+1$	0.3	0	0	0
	$0k0, k = 2n+1$	0.2	1	0	0
	$h0l, h = 2n+1$	0.3	20	0	0
260	$h00, h = 2n+1$	0.4	1	0	0
	$0k0, k = 2n+1$	0.2	0	0	0
	$h0l, h = 2n+1$	0.6	48	5	0
255	$h00, h = 2n+1$	0.7	4	1	0
	$0k0, k = 2n+1$	0.3	2	1	0
	$h0l, h = 2n+1$	1.5	139	38	18
250	$h00, h = 2n+1$	1.5	7	2	1
	$0k0, k = 2n+1$	0.2	1	0	0
	$h0l, h = 2n+1$	2.5	188	97	32
245	$h00, h = 2n+1$	1.1	8	1	0
	$0k0, k = 2n+1$	0.3	3	1	0
	$h0l, h = 2n+1$	2.4	197	94	30
104	$h00, h = 2n+1$	2.3	7	5	4
	$0k0, k = 2n+1$	0.2	0	0	0
	$h0l, h = 2n+1$	3.9	241	151	72

* Number of peaks violating the reported cut-off criterion